Supplemental Material : Topological Entanglement Across Quantum Phase Transition in Spin-Orbit coupled Bose-Einstein Condensate

Kashif Ammar Yasir,[1,2,*] Wu-Ming Liu,[3,†] and Gao Xianlong[1,‡]

[1] *Department of Physics, Zhejiang Normal University, Jinhua 321004, China.*
[2] *Zhejiang Institute of Photoelectronics, Jinhua 321004, China.*
[3] *Beijing National Laboratory for Condensed Matter Physics, Institute of Physics, Chinese Academy of Sciences, Beijing 100190, China*

(Dated: May 24, 2026)

* kayasir@zjnu.edu.cn
† wliu@iphy.ac.cn
‡ gaoxl@zjnu.edu.cn

I. EFFECTIVE NON-HERMITIAN HAMILTONIAN AND EQUIVALENCE WITH THE QUANTUM LANGEVIN APPROACH

In this section we detail how the microscopic Hermitian Hamiltonian of our system,

$$\hat{\mathcal{H}} = \int d\mathbf{r}\, \hat{\psi}^\dagger(\mathbf{r})\big(\hat{\mathcal{H}}_0 + \mathcal{V}\big)\hat{\psi}(\mathbf{r}) + \frac{1}{2}\int d\mathbf{r} \sum_{\sigma,\sigma'} \mathcal{U}_{\sigma\sigma'}\, \hat{\psi}^\dagger_\sigma \hat{\psi}^\dagger_{\sigma'} \hat{\psi}_{\sigma'} \hat{\psi}_\sigma + \hbar\Delta_c \hat{c}^\dagger \hat{c} - i\hbar\eta(\hat{c} - \hat{c}^\dagger), \tag{S1}$$

acquires an *effective* non-Hermitian character when the dissipative channelscavity photon leakage and atomic decayare incorporated. We show how these loss processes, introduced microscopically via the Lindblad master equation, generate a complex-valued Hamiltonian that governs the deterministic (no-jump) evolution of quantum trajectories, and how the same structure emerges naturally in the quantum Langevin formulation. Finally, we demonstrate how linearization yields a drift matrix whose complex spectrum encodes the observable non-Hermitian phenomena such as linewidth asymmetry, exceptional points, and topological winding.

A. Master equation and emergence of the effective non-Hermitian Hamiltonian

The open-system dynamics of the coupled cavityatom system are governed by the Lindblad master equation [S1, S2],

$$\dot{\hat{\rho}}(t) = -\frac{i}{\hbar}[\hat{\mathcal{H}}, \hat{\rho}] + \sum_j \mathcal{D}[\hat{L}_j]\hat{\rho}, \qquad \mathcal{D}[\hat{L}]\hat{\rho} \equiv \hat{L}\hat{\rho}\hat{L}^\dagger - \tfrac{1}{2}\{\hat{L}^\dagger\hat{L}, \hat{\rho}\}, \tag{S2}$$

where the dissipators $\mathcal{D}[\hat{L}_j]\hat{\rho}$ describe irreversible coupling to Markovian baths. For our system, the relevant jump operators are

$$\hat{L}_c = \sqrt{\kappa}\,\hat{c}, \qquad \hat{L}_{a,\sigma}(\mathbf{r}) = \sqrt{\gamma}\,\hat{\psi}_\sigma(\mathbf{r}), \tag{S3}$$

with κ and γ the photon and atomic decay rates, respectively.

Substituting Eq. (S2) and regrouping terms gives

$$\dot{\hat{\rho}} = -\frac{i}{\hbar}[\hat{\mathcal{H}}, \hat{\rho}] - \frac{1}{2}\sum_j \big(\hat{L}_j^\dagger \hat{L}_j \hat{\rho} + \hat{\rho}\,\hat{L}_j^\dagger \hat{L}_j\big) + \sum_j \hat{L}_j \hat{\rho} \hat{L}_j^\dagger. \tag{S4}$$

Defining the *effective non-Hermitian Hamiltonian*

$$\hat{H}_{\text{eff}} = \hat{\mathcal{H}} - \frac{i\hbar}{2}\sum_j \hat{L}_j^\dagger \hat{L}_j, \tag{S5}$$

the master equation becomes

$$\dot{\hat{\rho}} = -\frac{i}{\hbar}\big(\hat{H}_{\text{eff}}\hat{\rho} - \hat{\rho}\hat{H}_{\text{eff}}^\dagger\big) + \sum_j \hat{L}_j \hat{\rho} \hat{L}_j^\dagger. \tag{S6}$$

The deterministic part of the dynamics is thus generated by the non-Hermitian operator

$$\hat{H}_{\text{eff}} = \hat{\mathcal{H}} - \frac{i\hbar}{2}\left[\kappa\,\hat{c}^\dagger\hat{c} + \gamma\int d\mathbf{r} \sum_\sigma \hat{\psi}^\dagger_\sigma(\mathbf{r})\hat{\psi}_\sigma(\mathbf{r})\right], \tag{S7}$$

whose imaginary terms encode irreversible loss of excitation probability. Physically, $\hat{H}_{\text{eff}}$ describes the "no-jump evolution in the quantum trajectory picture [S6–S8]: the system evolves coherently but with decaying norm, while the stochastic quantum jumps $\hat{L}_j\hat{\rho}\hat{L}_j^\dagger$ restore total probability and account for emission events. This formal decomposition makes transparent how decay and loss transform a purely Hermitian system into one with an effective non-Hermitian structure whose spectral properties govern measurable linewidths and dynamical instabilities.

B. Heisenberg–Langevin correspondence and linearized drift matrix

An equivalent description emerges in the Heisenberg picture. Eliminating bath degrees of freedom in the Born-Markov approximation [S3–S5] yields the quantum Langevin equations,

$$\dot{\hat{c}}(t) = -\frac{i}{\hbar}[\hat{c}, \hat{\mathcal{H}}] - \frac{\kappa}{2}\hat{c}(t) + \sqrt{\kappa}\,\hat{c}_{\rm in}(t), \tag{S8}$$

$$\dot{\hat{\psi}}_\sigma(\mathbf{r}, t) = -\frac{i}{\hbar}[\hat{\psi}_\sigma(\mathbf{r}), \hat{\mathcal{H}}] - \frac{\gamma}{2}\hat{\psi}_\sigma(\mathbf{r}, t) + \sqrt{\gamma}\,\hat{\psi}_{\sigma,\rm in}(\mathbf{r}, t). \tag{S9}$$

Neglecting input noise terms, Eqs. (S8)(S9) correspond exactly to Schrdinger evolution under $\hat{H}_{\rm eff}$, demonstrating the equivalence of the Lindblad and Langevin approaches at the deterministic level. The inclusion of quantum noise operators $\hat{c}_{\rm in}, \hat{\psi}_{\rm in}$ restores the correct commutation relations and governs fluctuation spectra.

To study the linear response and spectral topology, we expand operators around their steady-state mean values:

$$\hat{c} = \bar{c} + \delta\hat{c}, \qquad \hat{\psi} = \bar{\psi} + \delta\hat{\psi}. \tag{S10}$$

Collecting the fluctuations into a vector $\delta\hat{\mathbf{X}}$, we obtain

$$\frac{d}{dt}\,\delta\hat{\mathbf{X}}(t) = K\,\delta\hat{\mathbf{X}}(t) + \hat{\boldsymbol{\xi}}(t), \tag{S11}$$

where $\hat{\boldsymbol{\xi}}(t)$ collects the Langevin noise terms and K is the non-Hermitian *drift matrix* whose elements are linear response coefficients derived from $\hat{H}_{\rm eff}$. Explicitly,

$$K = K_{\rm H} + K_{\rm D}, \qquad K_{\rm H}^\dagger = -K_{\rm H}, \quad K_{\rm D} = -\mathrm{diag}\left(\tfrac{\kappa}{2}, \tfrac{\gamma}{2}, \ldots\right), \tag{S12}$$

so that K inherits both coherent (anti-Hermitian) and dissipative (Hermitian) parts. Its eigenvalues,

$$\lambda_n = \omega_n - i\Gamma_n/2, \tag{S13}$$

encode collective oscillation frequencies ω_n and decay rates Γ_n, defining the systems linear stability and spectral response. The resolvent

$$G^R(\omega) = \left[-i\omega\mathbb{1} - K\right]^{-1}, \tag{S14}$$

determines the transmission, spectral density, and dynamical susceptibility, with poles directly revealing the non-Hermitian eigenmodes. In our SOCBEC system, these poles define linewidths and spectral asymmetries whose winding in complex parameter space identifies topological transitions.

For intuition, consider a two-mode truncation with effective Hamiltonian

$$H_{\rm eff}^{(2)} = \begin{pmatrix} \omega_c - i\frac{\kappa}{2} & g \\ g & \omega_a - i\frac{\gamma}{2} \end{pmatrix}. \tag{S15}$$

The eigenvalues

$$\lambda_\pm = \frac{\omega_c + \omega_a}{2} - i\frac{\kappa + \gamma}{4} \pm \sqrt{g^2 + \left(\tfrac{\omega_c - \omega_a}{2} - i\tfrac{\kappa - \gamma}{4}\right)^2}, \tag{S16}$$

illustrate explicitly how dissipation imbalance modifies hybridization and linewidths. When $\gamma > \kappa$, atomic decay dominates, producing asymmetric linewidths and eigenvalue coalescence at an exceptional point [S9, S10]. In the full many-body SOCBEC system, these exceptional structures generalize into non-Hermitian topological bands whose winding manifests as edge-localized resonances and enhanced entanglement, as analyzed in the main text.

Thus, starting from the microscopic Hermitian Hamiltonian (S1) and physically motivated Lindblad channels, we derive an effective non-Hermitian Hamiltonian (S7), or equivalently a drift matrix K, that captures the essential interplay between coherent coupling and dissipative imbalance. This formalism provides the theoretical foundation for interpreting the $\gamma > \kappa$ regime as a non-Hermitian topological phase, establishing a direct bridge between open-system quantum optics and the emerging field of non-Hermitian many-body physics.

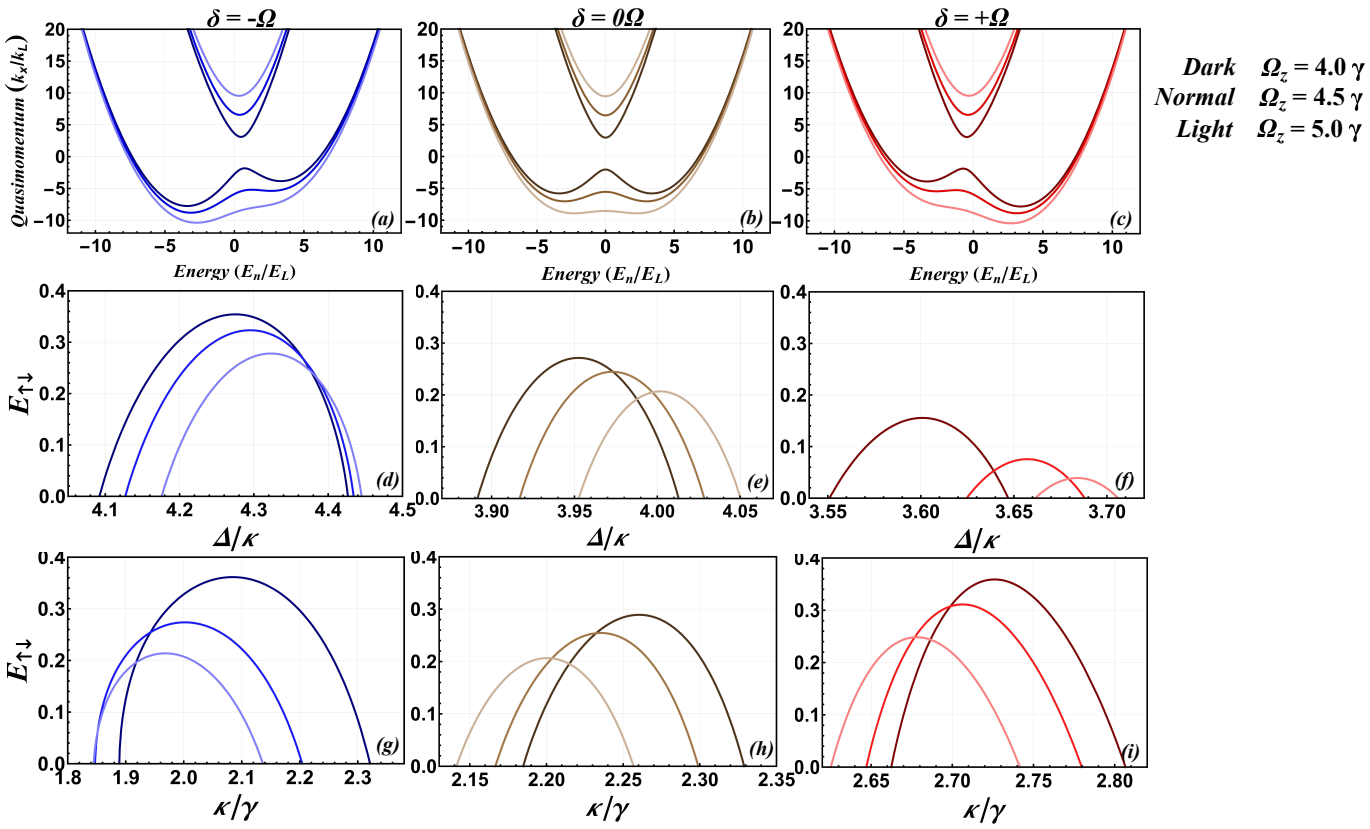

FIG. S1. (**a-c**) Eigenenergy spectra illustrated through quasimomentum k_x/k_L versus E_n/E_L for Raman detuning $\delta/\Omega = -1, 0, +1$, respectively, showing the double-well SOC dispersion that becomes asymmetric for non-zero detuning. (**d-f**) Corresponding bipartite entanglement $E_{\uparrow,\downarrow}$ between spin states as a function of detuning δ under different Raman couplings $\Omega_z/\gamma = 4.0$ (dark), 4.5 (normal), and 5.0 (light). (**g-i**) Entanglement $E_{\uparrow,\downarrow}$ versus dissipation ratio κ/γ for the same Ω_z sequence.

II. EIGENENERGY DISTRIBUTION AND ENTANGLEMENT

The first row of Fig. S1(**a-c**) illustrates the evolution of the SOC-BEC single-particle dispersions $E_{\pm}(q)$ with varying Raman detuning δ. At $\delta = 0$, the lower branch $E_{-}(q)$ exhibits a symmetric double-well structure centered at $\pm q_0$, corresponding to balanced spin-momentum coupling between the two pseudo-spin states. Introducing finite detuning breaks this symmetry: negative (positive) δ shifts the minimum of $E_{-}(q)$ toward $q < 0$ ($q > 0$), favoring one spin component and inducing spontaneous spin polarization. This asymmetric rearrangement defines the onset of a detuning-controlled phase transition in the SOC-BEC dispersion, separating the stripe-like mixed state from the planewave regime, as also observed in earlier Raman-coupled condensates [S11, S12].

The second row [Fig. S1(**d-f**)] displays the corresponding bipartite entanglement $E_{\uparrow,\downarrow}$ between the two pseudo-spin components. At zero detuning, $E_{\uparrow,\downarrow}$ attains a sharp maximum near the symmetric dispersion point where both spin branches are equally populated, signifying maximal hybridization between the spin modes. When δ becomes finite, this maximum shifts toward the energetically lower branch, producing an asymmetric entanglement distribution that directly mirrors the tilt in $E_{-}(q)$. As the Raman coupling Ω_z increases (dark→light curves), spin mixing is enhanced and the doublewell minima of $E_{-}(q)$ merge, resulting in a narrower entanglement peak and signaling the transition from the stripe/mixed to the plane-wave phase. Hence, $E_{\uparrow,\downarrow}$ functions as a direct quantum signature of the underlying SOCdriven structural transition: its peak position and width encode the competing effects of δ and Ω_z on the condensates internal spin coherence.

The last row [Fig. S1(**g-i**)] presents $E_{\uparrow,\downarrow}$ as a function of the dissipation ratio κ/γ for several Raman couplings Ω_z. In the trivial regime ($\kappa > \gamma$), photon loss dominates, suppressing coherence between the spin components and resulting in weak, diffuse entanglement characteristic of dispersive cavity-atom coupling. As γ exceeds κ, the atomic dissipation channel governs the dynamics, and $E_{\uparrow,\downarrow}$ rises sharply before saturating at larger γ/κ. This behavior reflects the emergence of spin-localized edge-like photonic modes: the loss imbalance modifies the drift spectrum such that cavity-generated fluctuations become confined near the pseudo-spin manifold, enabling enhanced correlation

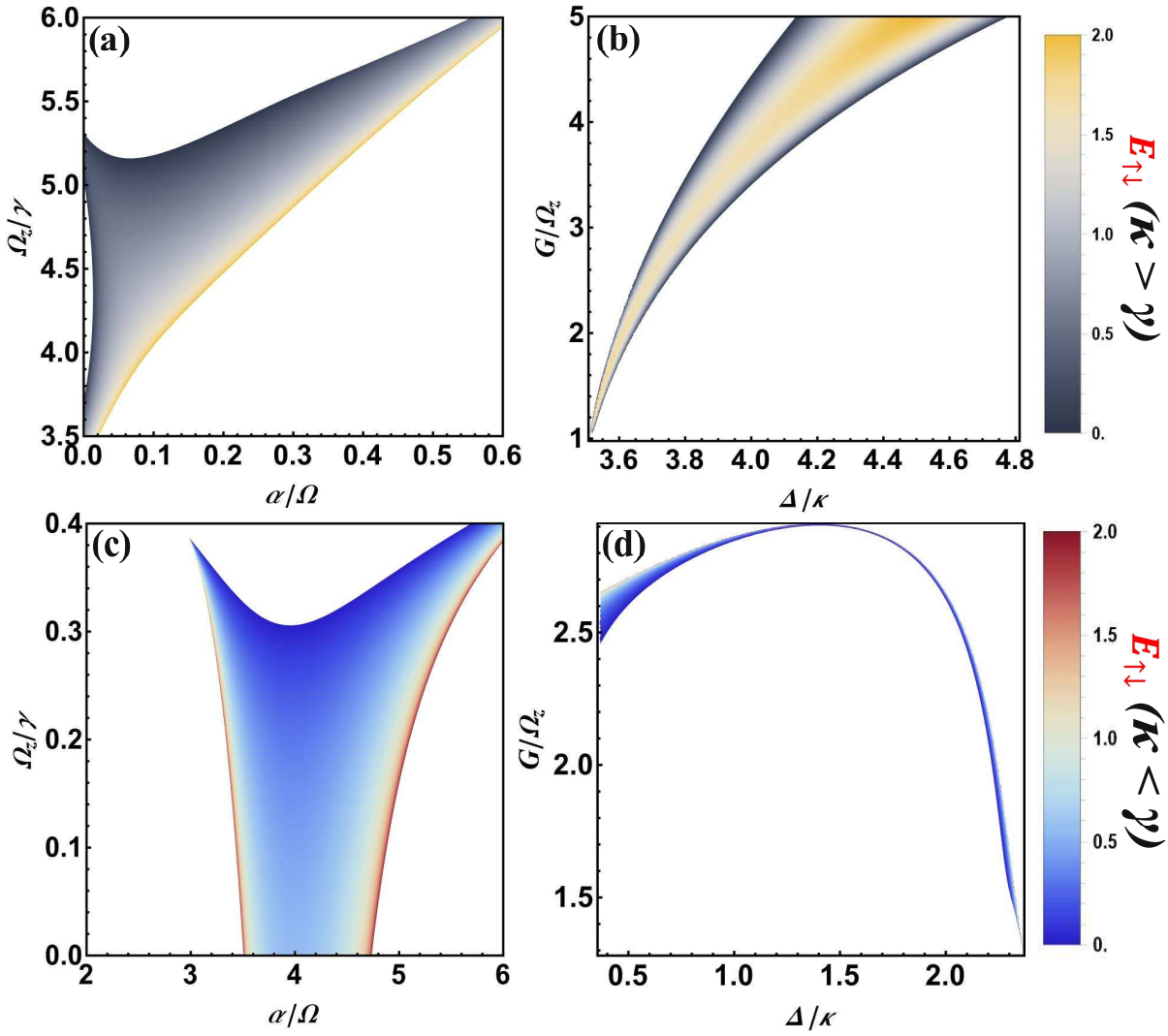

FIG. S2. Parameter maps of steady-state bipartite entanglement ($E_{\uparrow,\downarrow}$) in the (Ω_z, α) and (G, Δ) planes. (**a**,**b**) Trivial regime $\kappa > \gamma$: entanglement versus Raman coupling Ω_z and SOC strength α (**a**); and versus effective light-matter coupling $G = \sqrt{2} g_a |c_s|$ and cavity detuning Δ (**b**). (**c**,**d**) Non-trivial regime $\kappa < \gamma$: same parameter sweeps.

transfer. Physically, these edge resonances confine quantum fluctuations within the spin manifold, thus turning edge-mode localization into the mechanism that enhances coherent spin correlations. Together, the results of Fig. S1 demonstrate that Raman detuning and dissipation imbalance provide two independent, experimentally accessible control parameters for driving, enhancing, and stabilizing quantum entanglement in SOC-BEC confined in optical cavities.

III. ENTANGLEMENT PARAMETRIC CONFIGURATION

Figures S2(**a**,**b**) delineate how, in the dispersive (trivial) regime $\kappa > \gamma$, the bipartite spin-spin entanglement $E_{\uparrow,\downarrow}$ remains modest and is confined to narrow corridors of near-resonant hybridization. In the (Ω_z, α) plane [Fig. S2(**a**)], increasing either the Raman coupling Ω_z or the SOC strength α enhances spinmomentum locking and cavity-mediated exchange, producing a ridge of elevated $E_{\uparrow,\downarrow}$ along lines of roughly constant Ω_z/α. Below this corridor, weak Raman coupling undermixes the spin modes, while excessively strong Ω_z collapses the hybridization, leaving only residual dispersive correlations. A similar trend appears in the (G, Δ) plane [Fig. S2(**b**)], where entanglement peaks under nearresonant conditions ($|\Delta| \sim g_a N$) and moderate effective coupling G that compensates loss yet remains below the Routh-Hurwitz instability threshold. Large detuning or excessive G deters coherent exchange, reducing $E_{\uparrow,\downarrow}$ despite

stronger driving. Overall, in this regime, cavity-induced correlations are fragile, narrowband, and strongly dependent on resonance fine-tuning.

When the imbalance is inverted to $\kappa < \gamma$, as shown in Figs. S2(**c**,**d**), the same parameter sweeps yield qualitatively enhanced and broadened entanglement domains. In the (Ω_z, α) map [Fig. S2(**c**)], the previously narrow ridge expands into wide, high-contrast lobes, reflecting the onset of non-Hermitian coupling channels that sustain spinspin correlations across a broad parameter window. Here, the non-Hermitian imbalance reshapes the drift-matrix spectrum and stabilizes edge-modeassisted hybridization. In the (G, Δ) map [Fig. S2(**d**)], the entanglement maxima become taller and less sharply tuned to a single detuning value, owing to linewidth matching between cavity and atomic fluctuations induced by the non-Hermitian spectrum. However, beyond a critical G, the linear stability condition is again violated, and $E_{\uparrow,\downarrow}$ is suppressed in agreement with the Routh-Hurwitz constraints.

Together, the transition from Figs. S2(**a**,**b**) to Figs. S2(**c**,**d**) quantifies how replacing cavity-dominated loss ($\kappa > \gamma$) with atom-dominated dissipation ($\gamma > \kappa$) converts a weak, resonance-limited entangler into a robust, broadband generator of spin-spin and cavity-spin correlations. This evolution underscores the central insight of the main text: These maps show that tuning the loss hierarchy reshapes the correlation topology via non-Hermitian edge physics, converting dispersive coupling into edge-mode-enhanced spin entanglement. We now show how the quantum-Langevin treatment is equivalent to evolving under an effective non-Hermitian Hamiltonian H_{eff} obtained via the Lindblad master equation.

[S1] G. Lindblad, *Commun. Math. Phys.* **48**, 119130 (1976).
[S2] H.-P. Breuer and F. Petruccione, *The Theory of Open Quantum Systems* (Oxford Univ. Press, 2002).
[S3] C. W. Gardiner and M. J. Collett, *Phys. Rev. A* **31**, 37613774 (1985).
[S4] C. W. Gardiner and P. Zoller, *Quantum Noise*, 3rd ed. (Springer, 2004).
[S5] D. F. Walls and G. J. Milburn, *Quantum Optics* (Springer, 1994).
[S6] H. J. Carmichael, *An Open Systems Approach to Quantum Optics* (Springer, 1993).
[S7] J. Dalibard, Y. Castin, and K. Mølmer, *Phys. Rev. Lett.* **68**, 580583 (1992).
[S8] M. B. Plenio and P. L. Knight, *Rev. Mod. Phys.* **70**, 101144 (1998).
[S9] Y. Ashida, Z. Gong, and M. Ueda, *Rev. Mod. Phys.* **92**, 045005 (2020).
[S10] Z. Gong, Y. Ashida, K. Kawabata, K. Takasan, S. Higashikawa, and M. Ueda, *Phys. Rev. X* **8**, 031079 (2018).
[S11] Y.-J. Lin, K. Jimnez-Garca, and I. B. Spielman, *Nature* **471**, 8386 (2011).
[S12] V. Galitski and I. B. Spielman, *Nature* **494**, 4954 (2013).